

Experimental stress analysis of an arbitrary geometry containing irregularly shaped hole

B. Kalaycioglu¹  | A. Alshaya²  | R. Rowlands³ 

¹Mechanical Engineering Department, Kirikkale University, Kirikkale, Turkey

²Mechanical Engineering Department, Kuwait University, Kuwait City, Kuwait

³Mechanical Engineering Department, University of Wisconsin-Madison, Madison, Wisconsin, United States

Correspondence

R. Rowlands, University of Wisconsin-Madison, Madison, WI.
Email: rowlands@engr.wisc.edu

Funding information

International Post-Doctoral Research Fellowship

Abstract

Stresses can significantly influence the mechanical integrity of engineering structures. Motivated by prevalence of members containing cutouts, the objective of this paper is to demonstrate ability to stress analyse a finite, complicated-shaped plate containing an asymmetrical, irregularly shaped hole. Combining the load-induced temperature information with analytical and numerical tools provides the independent stresses full field, including on edges of the plate and adjacent to the top load. In addition to utilising real, rather than complex, variables, the technique smooths the recorded information, evaluates individual stresses, and requires neither differentiating the measured data nor knowing the elastic properties. Results are supported by those from a finite element analysis, force equilibrium, and strain gages.

KEYWORDS

complex geometry, concentrated loading, hybrid TSA

1 | INTRODUCTION

Shape optimization can be effective in minimising the weight of machine or structural members.^[1–3] Components such as bulkheads, automotive members, and wing ribs and spars consequently often involve nontraditional geometries and cutout configurations. The high stresses associated with such shapes can significantly influence reliability. Stress analyses of complicated geometries having irregularly shaped holes can be challenging as theoretical solutions tend to be restricted to simple infinite geometries, and like numerical methods, they require knowing the external loads. The latter are often unknown in practice. These difficulties motivate experimental approaches to such problems. However, it can be problematic to obtain reliable edge stresses by traditional experimental techniques. Moreover, fatigue analyses and strength criteria typically necessitate knowing the individual components of stress.

Acknowledging the above, this paper evaluates the individual stresses full field in a finite, arbitrarily-shaped plate containing an asymmetrical, irregularly shaped hole, Figure 1. This is achieved by processing the recorded load-induced

List of Symbols: $a_n, b_n, c_n, d_n; a'_n, b'_n, c'_n, d'_n; a_0, b_0, c_0, a_1, c_1, d_1, a'_1, c'_1, d'_1; A_0$, Airy coefficients; $[A]$, Airy Matrix; $\{c\}$, Vector of Airy coefficients; $\{d\}$, Vector of measured input data; $\{d'\}$, Vector of reconstructed/predicted data; E , Modulus of elasticity (Young's modulus); h , Number of imposed conditions on internal boundary; k , Number of Airy coefficients; K , Thermomechanical coefficient (TSA calibration coefficient); m , Number of measured TSA input values; N , Terminating integer of summation series; P , Load; r, θ , Polar coordinates; RMS, Root Mean Square; S , First stress invariant trace of stress tensor or isopachic stress ($=\sigma_1 + \sigma_2 = \sigma_{rr} + \sigma_{\theta\theta} = \sigma_{xx} + \sigma_{yy}$); S^* , Recorded thermoelastic signal; t , Number of imposed conditions on external boundary; x, y , Cartesian (rectangular) coordinates; α , Angle to normal of a point on edge of hole; Δ , Change; $\epsilon_{\eta\eta}$, Tangential strain; ν , Poisson's ratio; σ_o , Normalising stress based on gross, un-notched, area; $\sigma_1, \sigma_2, \sigma_3$, Principal stresses; $\sigma_{\xi\xi}, \sigma_{\eta\eta}, \sigma_{\xi\eta}$, Stresses in $\xi\eta$ -coordinates; $\sigma_{rr}, \sigma_{\theta\theta}, \sigma_{r\theta}$, Stresses in polar coordinates; $\sigma_{xx}, \sigma_{yy}, \sigma_{xy}$, Stresses in Cartesian coordinates; Σ , Summation; Φ , Airy stress function; ψ , Angle between the normal and polar r -direction, $(\alpha - \theta)$; ξ, η , Tangent-normal coordinate system; ∇^4 , Biharmonic operator; \backslash , Backslash operator (MATLAB)

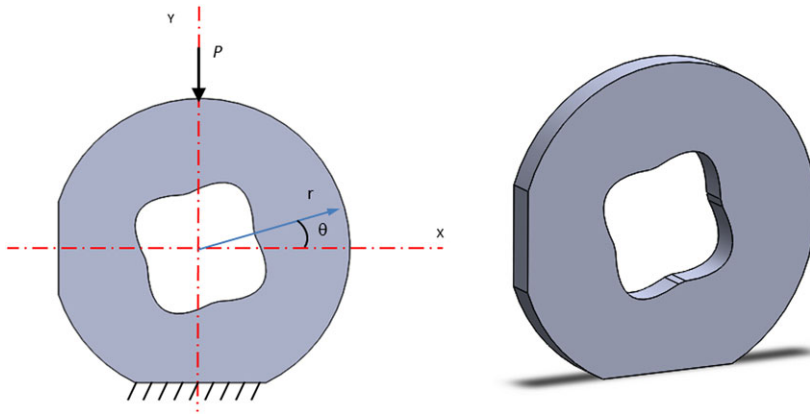


FIGURE 1 CAD model of arbitrary-shaped, finite plate containing an irregularly shaped hole

temperature information (frequently referred to as thermoelasticity or thermoelastic stress analysis or TSA) with analytical and numerical tools and applying the traction-free conditions on both the *internal* and *external* edges of the plate. Equilibrium and compatibility are satisfied. In addition to the technique's widespread applicability, the approach benefits from not having to know the material properties or external loading. The latter is important since external loads are often unknown in practice. The TSA results are validated independently.

The studies of Samad and Rowlands and Kurunthottikkal Philip and Rowlands^[4,5] analysed perforated rectangular plates. Contrasted with the present analysis, those previous studies did not account for the external boundary. Only stresses at and in the neighbourhood of the hole were consequently considered. The current analysis is complicated by the arbitrary external shape. Compatible with its more complicated geometry, traction-free conditions are applied on both of the external and internal edges of the plate. Unlike with the study of Samad and Rowlands^[4] or Kurunthottikkal Philip and Rowlands,^[5] determining stresses on the external boundary includes those adjacent to the top-applied load, P . The highly irregular geometry increases the amount of recorded TSA data employed, increased the form of the relevant stress function and substantially increases the required number of Airy coefficients. The arbitrary shape of the external edge of the plate, and having to consequently account for its boundary conditions, particularly aggravated the analysis. The authors are unaware of any previous TSA of a perforated geometry, which had to specifically account for both interior and exterior edges. For example, compared with the study of Kurunthottikkal Philip and Rowlands,^[5] the present analysis involves 10 times more recorded thermal input data and over four times as many Airy coefficients, that is, 103 (present study) versus 23 coefficients

For isotropic, elasto-static response in the absence of the body forces, stress equilibrium and strain compatibility give the following biharmonic Equation^[6]

$$\nabla^4 \Phi = 0, \quad (1)$$

where $\nabla^2 = \frac{\partial^2}{\partial r^2} + \frac{1}{r} \frac{\partial}{\partial r} + \frac{1}{r^2} \frac{\partial^2}{\partial \theta^2}$, and Φ is the Airy stress function. Although a reasonably simple general solution for the above equation is available in (real) polar coordinates, a comparable simple solution in real variables does not appear to exist in orthogonal curvilinear coordinates. Even if it did, to appropriately configure a full-field set of orthogonal coordinates compatible with the internal and external boundaries of a structure might not be trivial. Most stress analyses associated with highly complicated geometries employ complex variables and mapping techniques. Instead, the present use of polar coordinates offers the convenience and computational ease of real variables. Lacking a coordinate system aligned continuously with the current irregularly shaped boundaries, the polar stress components are transformed to those normal and tangential to the surface at discrete locations on the inner and outer edges to enable imposing the relevant local traction-free conditions.

Moiré, speckle, holography, grids, digital image correlation, photoelasticity, and strain gages are other candidate experimental approaches by which to stress analyse such structures. Displacement-based methods (e.g., moiré, speckle, holography, grids, and digital image correlation) necessitate differentiating the experimental data and knowing the elastic properties to obtain the strains/stresses. Differentiating measured data can be unreliable. Unlike displacement-based methods, TSA requires neither differentiating the measured information nor knowing the constitutive properties. Separating the individual stresses from birefringent data is non-trivial and time-consuming. Photoelastic time-edge stresses can also hamper determining reliable boundary stresses. Using strain gages necessitates constitutive properties, and the

gages provide information only at discrete locations. Mounting and electrically connecting the many strain gages needed to analyse throughout a region, and processing their output, can be onerous.

The authors are unaware of any previously published paper where experimental data were combined with analytical and/or numerical tools to evaluate the three independent components of stress full field in members, which have such a complicated shape as presently. The study of Kuske and Robertson^[7] photoelastically analysed structures containing square or rectangular holes having filleted corners. However, the technique required modelling the structure and its loading.

2 | THERMOELASTIC STRESS ANALYSIS

Thermoelastic stress analysis (TSA) is a non-contacting, non-destructive experimental method for determining the full-field stresses in loaded members. The technique enables the stress analysis of actual structures in their operating environment with a sensitivity comparable to that of strain gages. No surface preparation is required other than perhaps a flat black paint to provide an enhanced and uniform emissivity. The studies of Wong et al. and Stanley and Dulieu-Smith^[8,9] include some of the pioneering TSA contributions while the study of Greene et al.^[10] provides an overview of the method.

Under adiabatic conditions in elastic media subjected to proportional loading, the stress-induced recorded signal, S^* , is proportional to the change in the sum of the normal stresses, S (the stress invariant) at the point; that is,

$$S^* = K\Delta S = K\Delta(\sigma_1 + \sigma_2) = K\Delta(\sigma_{xx} + \sigma_{yy}) = K\Delta(\sigma_{rr} + \sigma_{\theta\theta}) = K\Delta(\sigma_{\xi\xi} + \sigma_{\eta\eta}), \quad (2)$$

where K is a calibration factor, and $\sigma_1, \sigma_2, \sigma_{rr}, \sigma_{\theta\theta}, \sigma_{xx}, \sigma_{yy}, \sigma_{\xi\xi}$, and $\sigma_{\eta\eta}$ are the normal stress components in the principal, polar, Cartesian rectangular coordinates, and normal and tangent to an edge, respectively. The load-induced temperature fluctuations are recorded by a sensitive infrared camera. Since derivation of the above equation assumes an adiabatic process,^[10] one typically loads the structure cyclically at a frequently high enough to satisfy adiabaticity. Although classical TSA provides information on only a linear combination of the stresses, engineering fatigue or failure theory analyses require knowing the magnitudes of the individual components of stress. There is consequently motivation to “separate the stresses.” The latter is achieved here by hybridising the stress-induced thermal data with analytical and numerical tools.

TSA-recorded data at and near edges are not reliable for two reasons: A pixel at an edge sees a spot, which is partly on the stressed structure and partly on the stress-free background, and the cyclic motion provides different data to the detector from different spatial positions. By using more values of S , together with other relevant and available information (i.e., analytical expressions associated with the traction-free conditions in Figure 2), than the number of Airy coefficients, the described hybrid TSA technique overcomes the challenges of noisy measured data and unreliable recorded information at and near edges to provide individual stresses reliably throughout the structure, including at the edges. Moreover, this is accomplished without knowing the external loading or material constitutive properties. Not having to know the external loads is very important since such are often not available in practical engineering problems. Because of the aforementioned practice of employing more side conditions (experimental values of S plus other relevant information) than the number of Airy coefficients, the latter are evaluated by least squares.

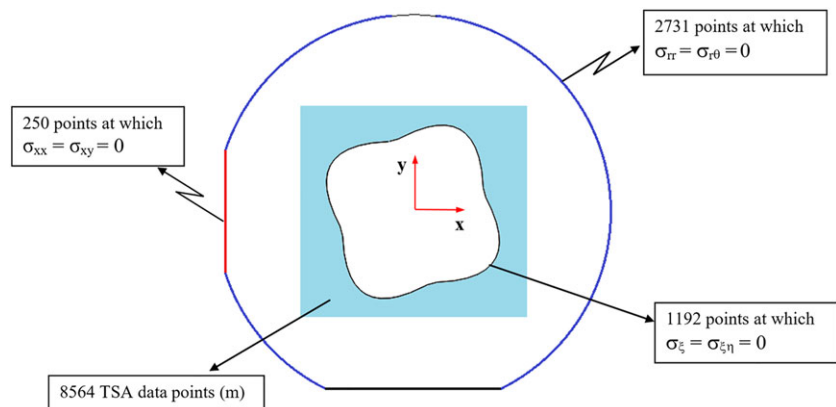


FIGURE 2 Locations and amount of TSA data and imposed boundary conditions (total of 16,910 input values)

3 | RELEVANT EQUATIONS

The relevant stress function for the current situation is^[6]

$$\begin{aligned}\Phi = & a_0 + b_0 \ln r + c_0 r^2 + A_0 \theta + \left(a_1 r + \frac{c_1}{r} + d_1 r^3 \right) \sin \theta + \left(a'_1 r + \frac{c'_1}{r} + d'_1 r^3 \right) \cos \theta \\ & + \sum_{n=2, 3, \dots}^N \left(a_n r^n + b_n r^{n+2} + c_n r^{-n} + d_n r^{-(n-2)} \right) \sin n \theta \\ & + \sum_{n=2, 3, \dots}^N \left(a'_n r^n + b'_n r^{n+2} + c'_n r^{-n} + d'_n r^{-(n-2)} \right) \cos n \theta,\end{aligned}\quad (3)$$

where r is the radial coordinate measured from the center of the hole, angle θ is measured counterclockwise from the horizontal x -axis (Figure 1), and N is the terminating index of the series. N can be any positive integer. The individual stress components in polar coordinates are available from

$$\sigma_{rr} = \frac{1}{r} \frac{\partial \Phi}{\partial r} + \frac{1}{r^2} \frac{\partial^2 \Phi}{\partial \theta^2}, \quad \sigma_{\theta\theta} = \frac{\partial^2 \Phi}{\partial r^2}, \quad \sigma_{r\theta} = -\frac{\partial}{\partial r} \left(\frac{1}{r} \frac{\partial \Phi}{\partial \theta} \right), \quad (4)$$

which give

$$\begin{aligned}\sigma_{rr} = & \frac{b_0}{r^2} + 2c_0 - \frac{2c_1}{r^3} \sin \theta + 2d_1 r \sin \theta - \frac{2c'_1}{r^3} \cos \theta + 2d'_1 r \cos \theta \\ & - \sum_{n=2, 3, \dots}^N \left\{ a_n n(n-1) r^{n-2} + b_n(n+1)(n-2) r^n + \right. \\ & \left. c_n n(n+1) r^{-(n+2)} + d_n(n-1)(n+2) r^{-n} \right\} \sin n \theta \\ & - \sum_{n=2, 3, \dots}^N \left\{ a'_n n(n-1) r^{n-2} + b'_n(n+1)(n-2) r^n + \right. \\ & \left. c'_n n(n+1) r^{-(n+2)} + d'_n(n-1)(n+2) r^{-n} \right\} \cos n \theta,\end{aligned}\quad (5)$$

$$\begin{aligned}\sigma_{\theta\theta} = & \frac{-b_0}{r^2} + 2c_0 + \frac{2c_1}{r^3} \sin \theta + 6d_1 r \sin \theta + \frac{2c'_1}{r^3} \cos \theta + 6d'_1 r \cos \theta \\ & + \sum_{n=2, 3, \dots}^N \left\{ a_n n(n-1) r^{n-2} + b_n(n+1)(n+2) r^n + \right. \\ & \left. c_n n(n+1) r^{-(n+2)} + d_n(n-1)(n-2) r^{-n} \right\} \sin n \theta \\ & + \sum_{n=2, 3, \dots}^N \left\{ a'_n n(n-1) r^{n-2} + b'_n(n+1)(n+2) r^n + \right. \\ & \left. c'_n n(n+1) r^{-(n+2)} + d'_n(n-1)(n-2) r^{-n} \right\} \cos n \theta,\end{aligned}\quad (6)$$

$$\begin{aligned}\sigma_{r\theta} = & \frac{A_0}{r^2} + \frac{2c_1}{r^3} \cos \theta - 2d_1 r \cos \theta - \frac{2c'_1}{r^3} \sin \theta + 2d'_1 r \sin \theta \\ & - \sum_{n=2, 3, \dots}^N \left\{ a_n n(n-1) r^{n-2} + b_n n(n+1) r^n - \right. \\ & \left. c_n n(n+1) r^{-(n+2)} - d_n n(n-1) r^{-n} \right\} \cos n \theta \\ & + \sum_{n=2, 3, \dots}^N \left\{ a'_n n(n-1) r^{n-2} + b'_n n(n+1) r^n - \right. \\ & \left. c'_n n(n+1) r^{-(n+2)} - d'_n n(n-1) r^{-n} \right\} \sin n \theta.\end{aligned}\quad (7)$$

Determining the individual stresses necessitates evaluating the unknown Airy coefficients in Equations (5) to (7). From Equations (5) and (6), one obtains

$$\begin{aligned}S = \sigma_{rr} + \sigma_{\theta\theta} = & 4c_0 + 8d_1 r \sin \theta + 8d'_1 r \cos \theta \\ & + \sum_{n=2, 3, \dots}^N \left\{ 4b_n(n+1) r^n - 4d_n(n-1) r^{-n} \right\} \sin n \theta \\ & + \sum_{n=2, 3, \dots}^N \left\{ 4b'_n(n+1) r^n - 4d'_n(n-1) r^{-n} \right\} \cos n \theta.\end{aligned}\quad (8)$$

Not all coefficients, which appear in the individual stress Equations (5) to (7) are present in Equation (8). It is, therefore, not possible to evaluate the individual Airy coefficients from only the recorded information, S^* . However, by additionally imposing the traction-free conditions on the internal and external edges of the plate, one is able to evaluate all of the coefficients in Equations (5) to (7) and, hence, the stresses. Equations (3) and (5)–(7) do not account for the load, P , so stresses based on them will not be applicable in the immediate vicinity of P .

4 | TRACTION-FREE CONDITIONS

The boundary conditions shown in Figure 2 were imposed discretely at multiple locations on the edge of the hole and on much of the traction-free portion of the external boundary of the plate.

4.1 | Internal boundary

Recognising that the hole is irregular in shape, a normal-tangential $\xi\eta$ -coordinate system (where ξ and η are the respective normal and tangent directions at a point), Figure 3, was used to impose the conditions on the edge of the hole. The stresses in $\xi\eta$ -coordinates were obtained from those in polar coordinates according to the following equation

$$\begin{Bmatrix} \sigma_{\xi\xi} \\ \sigma_{\eta\eta} \\ \sigma_{\xi\eta} \end{Bmatrix} = \begin{bmatrix} \cos^2\psi & \sin^2\psi & 2\sin\psi\cos\psi \\ \sin^2\psi & \cos^2\psi & -2\sin\psi\cos\psi \\ -\sin\psi\cos\psi & \sin\psi\cos\psi & \cos^2\psi - \sin^2\psi \end{bmatrix} \begin{Bmatrix} \sigma_{rr} \\ \sigma_{\theta\theta} \\ \sigma_{r\theta} \end{Bmatrix}, \quad (9)$$

which gives

$$\begin{aligned} \sigma_{\xi\xi} = & \frac{b_0}{r^2} \cos 2\psi + 2c_0 + \frac{A_0}{r^2} \sin 2\psi - \frac{2c_1}{r^3} \sin(\theta - 2\psi) + 2d_1 r (2\sin\theta - \sin(\theta + 2\psi)) \\ & - \frac{2c'_1}{r^3} \cos(\theta - 2\psi) + 2d'_1 r (2\cos\theta - \cos(\theta + 2\psi)) \\ & - \sum_{n=2,3,\dots}^N \left\{ \begin{aligned} & a_n n(n-1) r^{n-2} \sin(n\theta + 2\psi) + \\ & b_n(n+1) r^n [n \sin(n\theta + 2\psi) - 2 \sin n\theta] \\ & + c_n n(n+1) r^{-(n+2)} \sin(n\theta - 2\psi) + \\ & d_n(n-1) r^{-n} [n \sin(n\theta - 2\psi) + 2 \sin n\theta] \end{aligned} \right\} \\ & - \sum_{n=2,3,\dots}^N \left\{ \begin{aligned} & a'_n n(n-1) r^{n-2} \cos(n\theta + 2\psi) + \\ & b'_n(n+1) r^n [n \cos(n\theta + 2\psi) - 2 \cos n\theta] \\ & + c'_n n(n+1) r^{-(n+2)} \cos(n\theta - 2\psi) + \\ & d'_n(n-1) r^{-n} [n \cos(n\theta - 2\psi) + 2 \cos n\theta] \end{aligned} \right\}, \end{aligned} \quad (10)$$

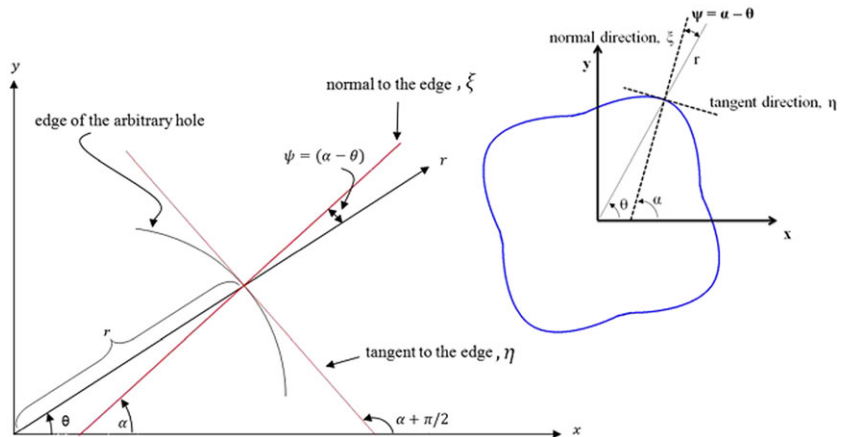


FIGURE 3 ξ - η coordinate system

$$\begin{aligned}
\sigma_{\xi\eta} = & -\frac{b_0}{r^2} \sin 2\psi + \frac{A_0}{r^2} \cos 2\psi + \frac{2c_1}{r^3} \cos(\theta - 2\psi) - 2d_1 r \cos(\theta + 2\psi) \\
& - \frac{2c'_1}{r^3} \sin(\theta - 2\psi) + 2d'_1 r \sin(\theta + 2\psi) \\
& - \sum_{n=2, 3, \dots}^N \left\{ \begin{array}{l} a_n n(n-1) r^{n-2} \cos(n\theta + 2\psi) + \\ b_n n(n+1) r^n \cos(n\theta + 2\psi) - \\ c_n n(n+1) r^{-(n+2)} \cos(n\theta - 2\psi) - \\ d_n n(n-1) r^{-n} \cos(n\theta - 2\psi) \end{array} \right\} \\
& + \sum_{n=2, 3, \dots}^N \left\{ \begin{array}{l} a'_n n(n-1) r^{n-2} \sin(n\theta + 2\psi) + \\ b'_n n(n+1) r^n \sin(n\theta + 2\psi) - \\ c'_n n(n+1) r^{-(n+2)} \sin(n\theta - 2\psi) - \\ d'_n n(n-1) r^{-n} \sin(n\theta - 2\psi) \end{array} \right\},
\end{aligned} \tag{11}$$

where $\psi = \alpha - \theta$ is the angle between the normal ξ - and polar r directions, Figure 3. As the edge of the hole is traction-free, the normal, $\sigma_{\xi\xi}$, and shear, $\sigma_{\xi\eta}$, stress expressions of Equations (10) and (11) were equated there to zero, that is; $\sigma_{\xi\xi} = \sigma_{\xi\eta} = 0$, Figure 2. Since the geometry of the hole is not defined by a simple mathematical equation, these boundary conditions cannot be satisfied analytically. Rather, they were imposed at discrete locations on the edge of the hole.

For any generic point on the edge of the hole having coordinates x and y , $\theta = \arctan\left(\frac{y}{x}\right)$, the tangential slope at the location gives angle α , hence $\psi = \alpha - \theta$, Figure 3.^[4] In order to determine the angle ψ along the boundary of the hole, multiple individual nodes (points) on the edge of the hole were first imported from the CAD model, Figure 4a. This was done at 1,192 essentially equally spaced boundary nodes. A developed subroutine was passed through each set of three neighbouring nodes along the edge to which a second-order polynomial was fitted, Figure 4b. Differentiating the polynomial analytically provided the slope (tangential direction η , hence angle, α) and consequently angle ψ at the middle node of the set of three neighbouring nodes. Repeating this process incrementally at overlapping sets of three neighbouring nodes along the edge gave the values of ψ at each of the discrete 1,192 nodes on the edge of the hole. Figure 4, which is a MATLAB plot of a portion of the edge of the hole, shows the nodes and identifies the tangential and normal directions.

4.2 | External boundary

Since the circular portion of the external boundary $r = R_{\text{outside}}$ away from the concentrated load, P , is traction-free, the radial, σ_{rr} , and shear, $\sigma_{r\theta}$, stress expressions of Equations (5) and (7) were each set to zero at 2,731 discrete points there,

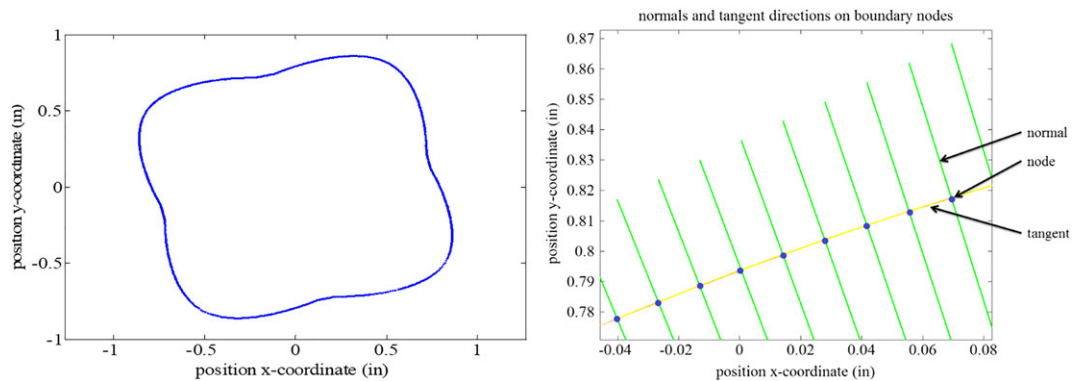


FIGURE 4 (a) Plot of internal boundary nodes (coordinates imported from CAD model); (b) Normal and tangent directions at points on a portion of edge of hole

Figure 2. However, because of the top load on the plate, no such conditions were imposed on the external edge at $85^\circ \leq \theta \leq 95^\circ$.

Stresses σ_{xx} and σ_{xy} were also set to zero at 250 discrete points on the traction-free left, vertical portion of the outside boundary, Figure 2. For that, the relevant Cartesian components of stresses were evaluated from the polar stresses according to the following transformation expression

$$\begin{Bmatrix} \sigma_{xx} \\ \sigma_{yy} \\ \sigma_{xy} \end{Bmatrix} = \begin{bmatrix} \cos^2\theta & \sin^2\theta & -2\sin\theta\cos\theta \\ \sin^2\theta & \cos^2\theta & 2\sin\theta\cos\theta \\ \sin\theta\cos\theta & -\sin\theta\cos\theta & \cos^2\theta - \sin^2\theta \end{bmatrix} \begin{Bmatrix} \sigma_{rr} \\ \sigma_{\theta\theta} \\ \sigma_{r\theta} \end{Bmatrix}, \quad (12)$$

where θ is the polar angle between the radial direction, r , and x -axis, Figure 1.

5 | EXPERIMENTAL SETUP

5.1 | Plate preparation and loading

Figure 5 contains the dimensions of the aluminium (6061-T6, ultimate strength between 275 and 311 MPa, yield stress between 241 and 275 MPa; Wiedenbeck, Inc., Madison, WI) plate. Material properties are $E = 70$ GPa and $\nu = 0.33$. The specimen was initially polished very lightly with 400-grid emery cloth. A coating of Krylon Ultra-Flat black paint was then applied to provide an enhanced and uniform thermal emissivity. Precautions were taken when polishing the face of the plate not to round-off the edges as this could further erode the quality of adjacent thermal information. The plate was vertically compressed cyclically at 1334.46 ± 667.23 N (300 ± 150 lb) in a 20-kp (53.3 kN) capacity MTS hydraulic

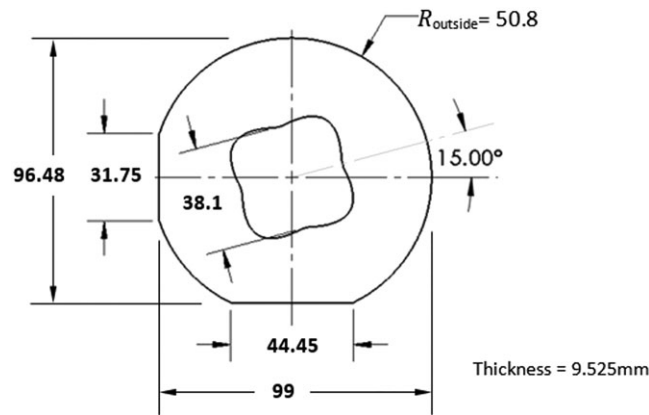


FIGURE 5 Dimensions (in mm) of the plate



FIGURE 6 Experimental setup

testing machine, Figure 6. The loading ratio (maximum-to-minimum force) was consequently 3. A piece of comparatively compliant wood was located between the bottom of the plate and the bottom loading platen to encourage uniform loading there and minimise heat conduction from the bottom of the plate, Figure 6. The plate was loaded cyclically at 20 Hz, and the load-induced TSA data were recorded. The selection of 20 Hz was based on over 25 years of relevant TSA experience as well as verifying experimentally that the response was adiabatic.

5.2 | TSA recording and calibration

The thermal information was recorded with a commercial sensitive infrared camera (DeltaTherm DT1400; Stress Photonics, Madison, WI). The camera employs an indium antimonide (InSb) focal-plane array, which responds in the 3–5 μm range with a peak response at a wavelength of 5.3 μm . Camera detectors are cooled to 77 K with liquid nitrogen. The camera records at 1,000 frames/s, and the system provides images of surface temperature variations with a resolution of 0.001°C. TSA images were captured and averaged over two minute durations, and then exported to Excel to convert each pixel into a data point, that is, 256 by 256 matrix, 65,536 data points, Figure 7. Pixel size is 0.46 mm (0.018"). Recognising the unreliable thermoelastic data on or near an edge, no recorded TSA information was used within at least two pixel positions (0.92 mm) of the inner edge of the plate and much further from the outer boundary. The phase information was also monitored to ensure that adiabatic conditions prevailed.

The thermoelastic coefficient K was evaluated from a separate uniaxial tensile specimen of the same material, thickness, and coating of the flat black paint and cyclically loaded at the same frequency (20 Hz) on the same day as the

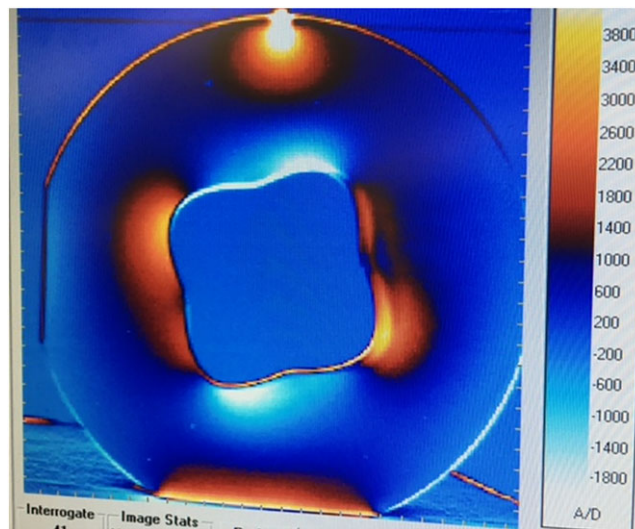


FIGURE 7 Recorded TSA signal, S^* , in aluminium plate loaded at a range of 1,334 N and frequency 20 Hz

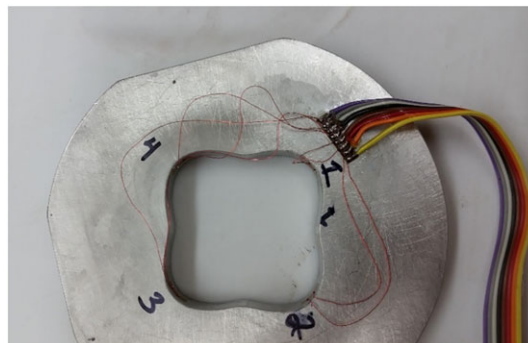


FIGURE 8 Strain-gaged plate

perforated plate. The thermoelastic coefficient was determined to be $K = 178.4 \text{ U/MPa}$ (1.23 U/psi). The unit U is used to signify the raw TSA output is in uncalibrated signal units.

5.3 | Strain gages

The perforated plate was strain-gaged, Figure 8, and the results from which are compared with the TSA-determined strains at a static load of $1,334.46 \text{ N}$ (300 lb). The commercial foil strain gages were mounted on the transverse, curved surface of the hole at each of $\theta = 58^\circ, 158^\circ, 232^\circ$, and 338° of Figure 1. The four, single-element strain gages (EA-06-015DJ-120 by Vishay Micro-Measurements) have a gage resistance of $120.0 \pm 0.3\% \Omega$ and a gage factor of $2.05 \pm 1.0\%$ Figure 8.

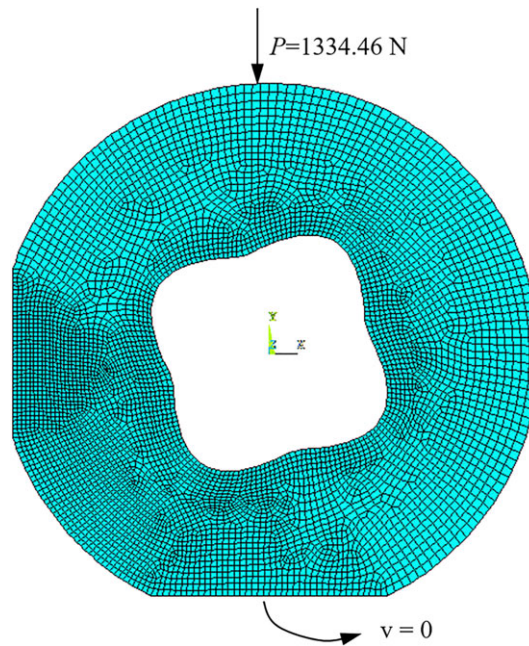


FIGURE 9 FE model with loading and displacement conditions

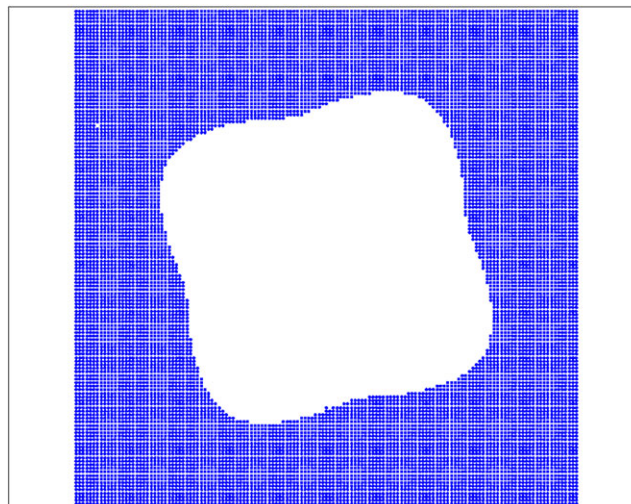


FIGURE 10 Source locations of $m = 8,564$ employed S^* values

5.4 | Finite element analysis

Also, for comparison with the TSA, a finite element analysis (FEA) prediction using ANSYS was prepared of the plate of Figure 1 and the elastic properties of $E = 70$ GPa and $\nu = 0.33$. A concentrated load of 1,334.46 N (300 lbs) was applied at a top of the plate, and roller constraint (assuming no vertical motion) was applied along the bottom of the plate. Plane 183 isoparametric element with eight nodes were employed. A convergence test was applied until the change in results of maximum stress between two successive meshing was less than 2%. The FE model utilises 2,934 elements and 6,076 nodes, Figure 9.

5.5 | Data processing

The measured TSA data were digitalised in a matrix form and combined with the Airy stress function to help determine the individual stresses. The unreliable TSA data at and near the edges were not used. The source locations of the utilised 8,564 values of S^* are shown in Figure 10.

Like most experimental data, the recorded S^* incorporates some noise. It is, therefore, advantageous to have more conditions available than number of unknown Airy coefficients and to evaluate the coefficients using least squares. As such, with reference to Figure 2, there are $m = 8,564$ thermally determined values of S in Equation (8), plus $h = 2 \times 1192 = 2,384$ internal edge conditions (i.e., $\sigma_{\xi\xi} = \sigma_{\xi\eta} = 0$ in Equations 10 and 11), plus $t = 2 \times (2731 + 250) = 5,962$ external edge conditions (i.e., $\sigma_{rr} = \sigma_{r\theta} = 0$) at 2,731 locations on the round portion in Equations (5) and (7) and $\sigma_{xx} = \sigma_{xy} = 0$ at 250 points along the left vertical edge in Equation (12) for a total of 16,910 side conditions with which to evaluate the Airy coefficients. From the recorded thermoelastic data and these locally imposed boundary conditions, these coefficients were evaluated from the following linear system of equations

$$[A]_{(m+h+t) \times k} \{c\}_{k \times 1} = \{d\}_{(m+h+t) \times 1} \quad (13)$$

or rewritten as

$$\begin{bmatrix} S \\ \vdots \\ \sigma_{\xi}(at \text{ edges}) \\ \vdots \\ \sigma_{\xi\eta}(at \text{ edges}) \end{bmatrix} = \begin{bmatrix} S_{TSA} \\ \vdots \\ 0 \\ \vdots \\ 0 \end{bmatrix} = \begin{bmatrix} 0 & \dots & \dots & -4(n-1)r^{-n} \cos(n\theta) \\ \vdots & & \vdots & \vdots \\ \frac{\cos 2\psi}{r^2} & \dots & \dots & (n-1)r^{-n} \begin{bmatrix} \cos n\theta(-n \cos 2\psi - 2) \\ -2n \sin n\theta \cos\psi \sin\psi \end{bmatrix} \\ \vdots & & \vdots & \vdots \\ \frac{-2 \sin\psi \cos\psi}{r^2} & \dots & \dots & n(n-1)r^{-n} \begin{bmatrix} 2 \cos n\theta \sin\psi \cos\psi \\ + \sin n\theta \cos 2\psi \end{bmatrix} \end{bmatrix} \begin{bmatrix} b_o \\ \vdots \\ \vdots \\ \vdots \\ d'_n \end{bmatrix}, \quad (14)$$

where $m = 8,564$ is the total number of measured values of $S \left(= \frac{S^*}{K} \right)$, $h = 2 \times 1192 = 2,384$, and $t = 2 \times (2731 + 250) = 5,962$ are the number of the imposed conditions on the internal and external boundaries, and k is the number of unknown Airy coefficients. Matrix $[A]$ consists of the m analytical expressions of stress tensor, S , of

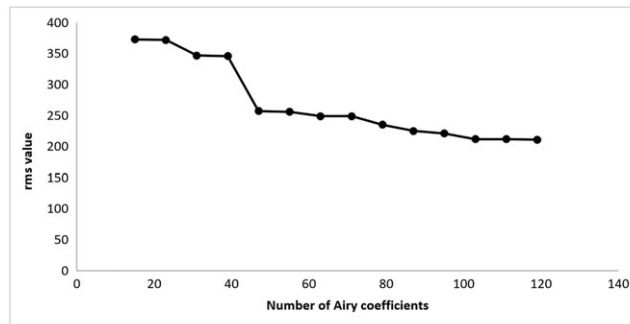


FIGURE 11 RMS values versus the number of coefficients, k

Equation (8), plus $h + t$ traction-free boundary conditions on the internal and external boundaries. The vector $\{c\}$ contains the k unknown Airy coefficients, and vector $\{d\}$ contains the m experimental TSA data plus the $h + t$ zeros associated with the traction-free edge conditions at the relevant locations as in [A]. The number of equations, $m + h + t = 16,910$ exceeds the number of coefficients, k .

One must evaluate how many Airy coefficients to retain. Too few coefficients will produce inaccurate results while too many can cause the Airy matrix to become unstable or even singular due to computer round-off and quantization errors. The amount of measured input data needed can also depend on the value of k , as more coefficients could necessitate more experimental values of S . The number of Airy coefficients to retain was assessed by monitoring the condition number of the respective Airy matrices and computing the Root Mean Square (RMS) for a series of different number of Airy coefficients, as well as by comparing reconstructed and the experimental thermoelastic information. The RMS represents the discrepancy between the calculated thermoelastic data, $\{d'\}$, from Equation (13) and the experimental information plus the imposed traction-free edge conditions, $\{d\}$. Multiplying the original matrix $[A]$ by the least-squares evaluated values, $\{c\}$ gives the calculated vector $\{d'\}$, which is typically not exactly the same as $\{d\}$. The RMS was computed according to

$$(\mathbf{d}' - \mathbf{d})_{rms} = \sqrt{\sum_{i=1}^{m+h+t} \frac{(d'_i - d_i)^2}{m + h + t}}, \quad (15)$$

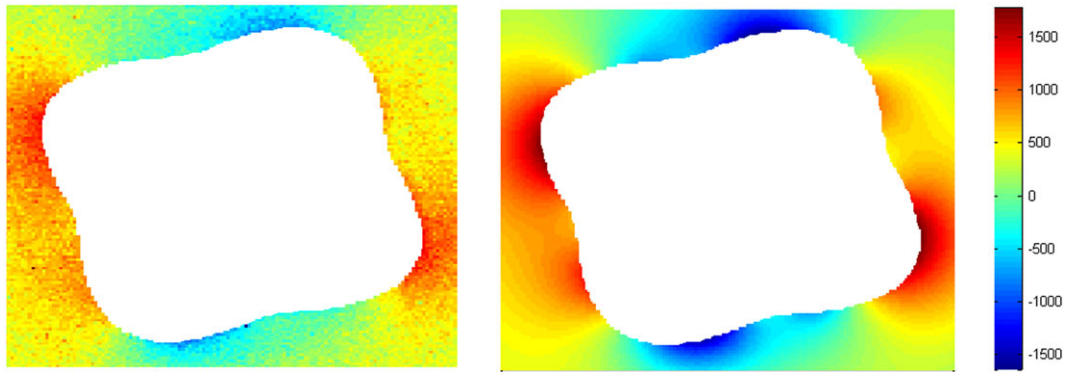


FIGURE 12 Contour plots of S^* from experimental TSA (left) and reconstructed based on the hybrid method (right), $k = 103$ and $m + h + t = 16,910$

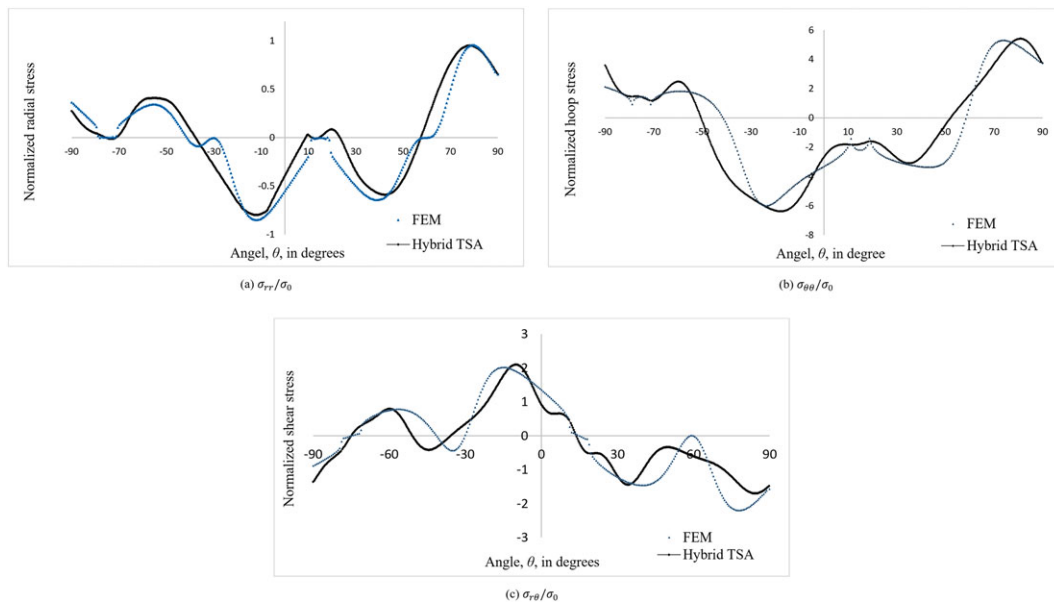


FIGURE 13 (a) Radial, (b) hoop, and (c) shear stresses on edge of hole from FEM and hybrid TSA ($k = 103$ and $m + h + t = 16,910$)

where $m + h + t = 16,910$ is the total number of quantities in vector $\{d\}$. It is desirable to use the smallest number of coefficients that gives sufficient accuracy. In addition to requiring potentially more experimental input data, employing more coefficients than necessary can increase computational time and the condition number of the Airy matrix. The latter could increase the chances of the $[A]$ matrix becoming singular. The condition number of an $[A]$ matrix with respect to an argument measures how much the output value of that matrix can change for a small change in the input argument. This information is used to measure how sensitive the matrix is to changes or errors in the input and how much error in the output results from an error in the input.

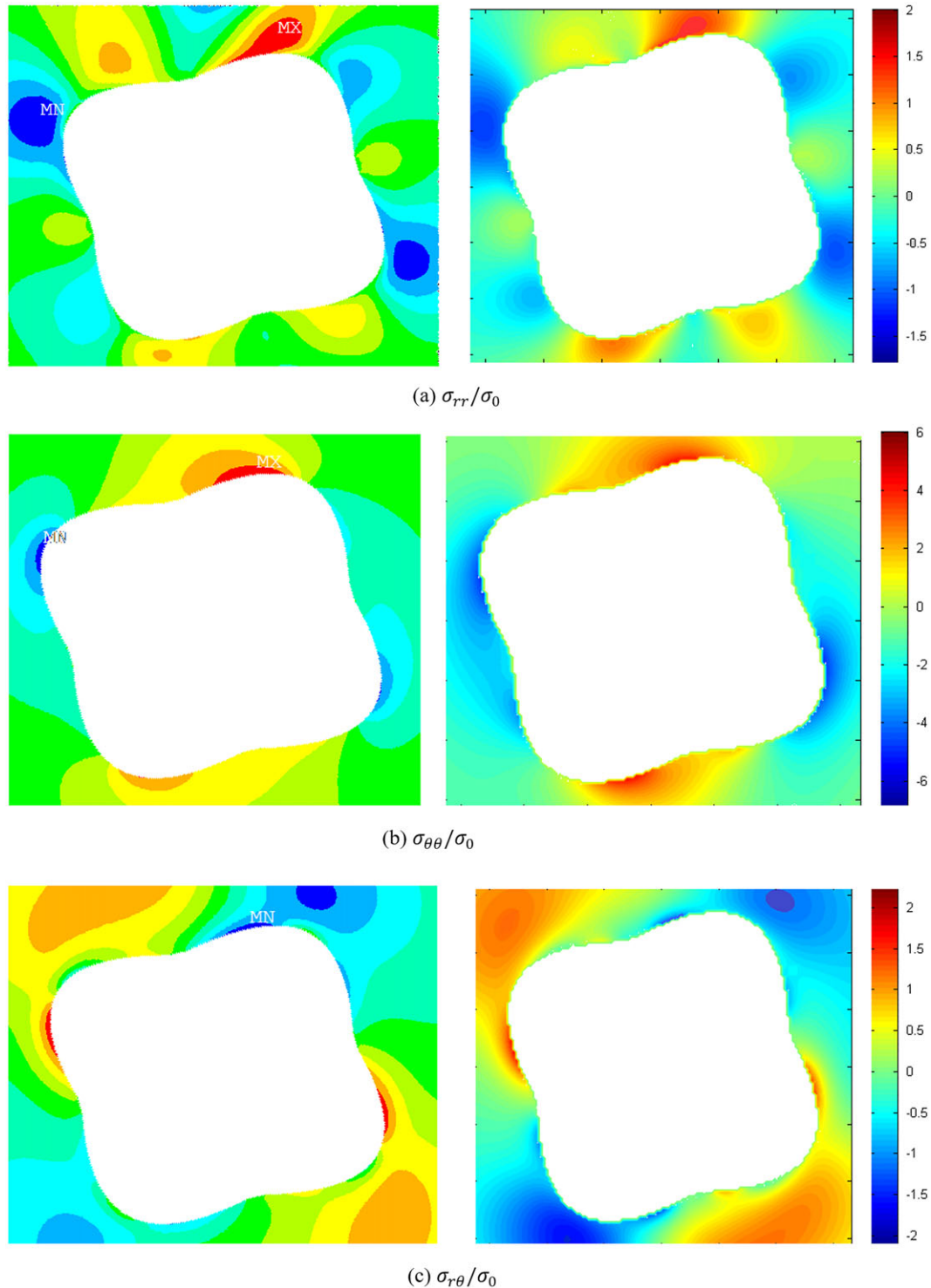


FIGURE 14 Contour plots of polar stresses from FEM (left) and hybrid-TSA ($k = 103$ and $m + h + t = 16,910$; right)

Figure 11, based on the $m + h + t = 16,910$ side conditions, suggests using $k = 103$ coefficients. The RMS does not improve beyond $k = 103$. The results of Figure 12, which compares experimental and reconstructed (according to $\{d\}' = [A]\{c\}$) contours of S^* , supports the appropriate use of 103 coefficients. Having decided how many coefficients to employ, their magnitudes were determined from Equation (14) by least squares using the backslash “\” in MATLAB.

6 | RESULTS

6.1 | Thermoelastic

The TSA-determined stresses are compared with FEM predictions in Figures 13–16. Figure 13 compares the stresses on the edge of the hole, and Figure 14 contains contour plots. Since $\sigma_{\xi\xi}$ and $\sigma_{\xi\eta}$ are numerically zero on the edge of the hole as dictated by imposing the traction-free conditions there, σ_{rr} and $\sigma_{r\theta}$ are small compared with $\sigma_{\theta\theta}$. Figure 15 shows the tangential stress, $\sigma_{\eta\eta}/\sigma_0$, (from TSA, FEM and strain gages) on the edge of the hole whereas Figure 16 contains the stress $\sigma_{\theta\theta}/\sigma_0$ on the circular portion of the external boundary. Stress reliability there is quite good even though no TSA data were employed approaching the outer edge of the plate. No boundary conditions were applied on the external edge at $85^\circ \leq \theta \leq 95^\circ$, and Equations (5)–(7) do not incorporate Flamant-type stresses associated with the top load. However, the recorded thermal information of Figure 7 does reflect the influence of the top applied load, and the stress of Figure 16 beyond the immediate neighbourhood of P is compatible with expectations. As anticipated, the results of Figures 13b and 15 are quite similar. All actual stresses are normalised with respect to the nominal stress, $\sigma_0 = 1,334.46/(99 \times 9.53) = 1.415$ MPa (205.2 psi). Based on results of Figure 15, the largest stress on the edge of the hole is well below the yield point of the aluminium. Upon unloading, there was also no indication of yielding at the top loading location.

6.2 | Force equilibrium

To further assess reliability of the present method, force equilibrium based on TSA-determined stress was compared with the physically applied load. This was done by numerically integrating the vertical stress σ_{yy} along the line $y = 0$ in Figure 1, that is,

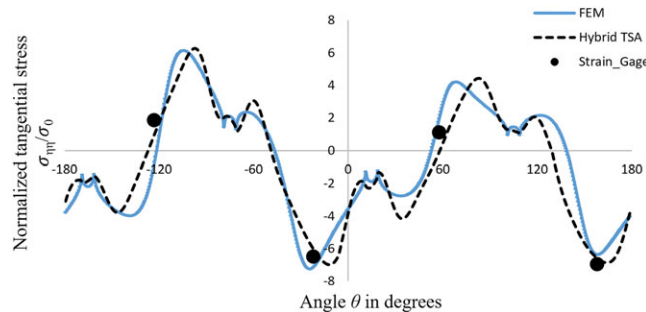


FIGURE 15 Tangential stress, $\sigma_{\eta\eta}/\sigma_0$, on edge of hole from FEM, strain gages, and hybrid TSA ($k = 103$ and $m + h + t = 16,910$)

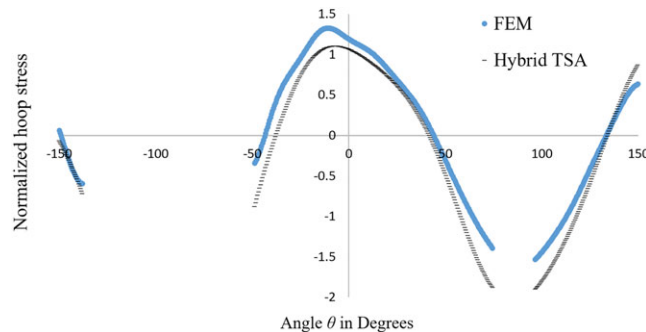


FIGURE 16 Hoop stress, $\sigma_{\theta\theta}/\sigma_0$, on circular portion of external edge of plate from FEM and hybrid TSA ($k = 103$ and $m + h + t = 16,910$)

$$P = \int \sigma_{yy} dA = \int \sigma_{yy} t dx, \quad (16)$$

where t is the plate thickness. The calculation involved integrating a fourth order polynomial representation of individual discrete values of the TSA-determined stress σ_{yy} of Equation (12) along $y = 0$. The computed load based on hybrid-TSA stress is 1.38 kN (310.8 lb), which agrees within 3.6% of the actual physically applied load of 1.33 kN (300 lb).

7 | SUMMARY, DISCUSSION, AND CONCLUSIONS

This paper determines the three independent stresses full field in a finite, complicated-shaped member containing an asymmetrical, irregularly shaped hole by processing the load-induced temperature information with a stress function and discretely imposing available traction-free conditions. The analysis enjoys the convenience of polar, rather than necessitating general curvilinear, coordinates, or using complex variables and mapping techniques. Engineers, particularly, tend to be more comfortable with real, rather than complex, variables. It is unnecessary to know either the material's constitutive properties or the external loading. Unlike displacement-based experimental techniques, the method does not require knowing the constitutive properties or differentiating the measured data. Although recorded thermal information on and near edges is unreliable, the discussed approach provides accurate stresses on both the inner and outer edges of the tested structure. Equilibrium and compatibility are satisfied.

The top external edge of the plate is subjected to a load, P , but the stress function of Equation (3), and hence, the expressions for the stresses do not account for P . However, the recorded thermal information does capture the influence of P . The tangential stress on the top edge in Figure 16 includes that in the neighbourhood of, but not under or immediately adjacent to, P . Notwithstanding the stress function does not include P , and the consequent effects on the stresses, the TSA-determined stress distribution throughout $50^\circ \leq \theta \leq 135^\circ$ in Figure 16 is compatible with expectations. While the FEM prediction is based on a point/line load, the top loading of the TSA experiment actually involves a distribution over a small but finite area. That the TSA result exceeds that by FEM at $50^\circ \leq \theta \leq 135^\circ$ is perhaps at least partly due to Equation (3) not accounting for P . For a highly brittle material, which is particularly weak in compression, it could be prudent to augment Equation (3) to include the contribution from P .

The current geometry and loading enable one to obtain reliable FEM results against which to assess reliability of the experimental results. However, the hybrid-TSA method is applicable to more complicated problems, which are difficult for FEM. For example, while industry makes prevalent use of FEM, strain gages are often employed in that environment to obtain the boundary conditions for the FEA.

The hybrid concepts can be used with other measured information. Although the present plate was loaded in the laboratory, previous studies^[11–14] illustrate abilities to determine stresses thermoelastically under much more general environments. The current analysis involves a finite plate, but the concepts are extendable to infinite geometries by omitting those Airy coefficients, which would give infinite stresses as r approaches infinity. The value obtained by integrating the TSA-determined values of σ_{yy} across the relevant area, and its comparison with the physically applied load, is employed here to assess the reliability of the current TSA method. Such a calculation demonstrates how experimentally determined stress information could be used to evaluate applied loads if the latter were not known, that is, provide an effective inverse method.

A major contribution of this paper is the demonstrated ability to determine the individual stresses full field, including those on the inner and outer edges, of perforated structures having highly irregularly internal and external geometries. This study is believed to be the most complicated and comprehensive, and yet most general, thermoelastic stress analysis to date. The good agreement between the present TSA results and those from FEA, force equilibrium, and the strain gages provides strong confidence in the ability to obtain reliable stresses from recorded thermal information in such situations.

ACKNOWLEDGEMENT

Dr. B. Kalaycioglu acknowledges the financial support of an International Post-Doctoral Research Fellowship from The Scientific and Technological Research Council of Turkey, Turkey, and Kirikkale University, Turkey which enabled him to spend two years at the University of Wisconsin-Madison, Madison, WI, USA.

ORCID

B. Kalaycioglu  <https://orcid.org/0000-0002-1295-3816>

A. Alshaya  <https://orcid.org/0000-0002-9105-5300>

R. Rowlands  <https://orcid.org/0000-0002-0991-8059>

REFERENCES

- [1] J. H. Zhu, W. H. Zhang, L. Xia, *Arch. Comput. Methods Eng.* **2016**, 23(4), 595.
- [2] B. K. Stanford, P. D. Dunning, *J. Aircr.* **2014**, 52(4), 1298.
- [3] C. Li, I. Y. Kim, *Proc. Inst. Mech. Eng. Part J. Automob. Eng.* **2015**, 229(10), 1361.
- [4] W. A. Samad, R. E. Rowlands, *Exp. Mech.* **2014**, 54(3), 457.
- [5] S. Kurunthottikkal Philip, R. E. Rowlands, *Jour. Mechanics Engineering & Automation* **2017**, 7(3), 145.
- [6] R. W. Soutas-Little, *Elasticity*, Dover Publications, Mineola, NY **1999**.
- [7] A. Kuske, C. Robertson, *Photoelastic stress analysis*, John Wiley & Sons Ltd, London **1974**.
- [8] K. Wong, J. G. Sparrow, S. A. Dunn, *Jour. Phys. Chem. Solids* **1988**, 49(4), 395.
- [9] P. Stanley, J. M. Dulieu-Smith, *Exper. Tech.* **1996**, 20(2), 21.
- [10] R. J. Greene, E. A. Patterson, R. E. Rowlands, Thermoelastic stress analysis, in *Handbook of experimental solid mechanics*, (Ed: W. Sharpe), Springer **2007** 743.
- [11] R. W. Wolfe, R. E. Rowlands, C. H. Lin, *Tech. Exp. Mech. Appl. For. Prod. Res.* **1994**, 23.
- [12] S. T. Lin, J. P. Miles, R. E. Rowlands, *Exp. Mech.* **1997**, 37(3), 225.
- [13] T. Sakagami, Y. Izumi, N. Mori, S. Kubo, *Quant. InfraRed Thermography* **2010**, 7(1), 73.
- [14] R. Tighe, J. Dulieu-Barton, J. P. Tyler and S. Lormor, "On-site application of thermoelastic stress analysis using vibration loading". Society of Experimental Mechanics Annual Conference, **2016**.

How to cite this article: Kalaycioglu B, Alshaya A, Rowlands R. Experimental stress analysis of an arbitrary geometry containing irregularly shaped hole. *Strain*. 2019;e12306. <https://doi.org/10.1111/str.12306>